UNIVERSITY OF CALIFORNIA
RIVERSIDE

Simulation of a Photocatalytic Microreactor with COMSOL Multiphysics

A Thesis submitted in partial satisfaction
of the requirements for the degree of

Master of Science

in

Mechanical Engineering

by

Kairui Xia

September 2018

Thesis Committee:
Dr. Masaru P. Rao, Chairperson
Dr. Marko Princevac
Dr. Ming Liu

The Thesis of Kairui Xia is approved:

_____

_____

_____

Committee Chairperson

University of California, Riverside

ACKNOWLEDGMENTS

I would first like to thank my thesis advisor and PI Dr. Rao who gave me a precious opportunity to become a research member under his advisement. One year ago, I was not sure about what to do after finishing two quarters of graduate class study, then I was attracted by Dr. Rao's MEMS class and it was amazing that I could join his lab later. This one-year research experience taught me how to do research and what an engineer should be like which I did not know well before joining the lab. Thank you for advising and encouraging me during this one year and I am really looking forward to working with you in the future.

I would also like to thank all the colleagues in the Biomedical Microdevices Laboratory, Duncan Ashby, Bryan Woo, Harish Dixit, Samantha Corber, Benjamin Sommerkorn, Edver Bahena, Ryan Peck and Sanika Nishandar for helping and supporting me whenever I got lost while doing research. And I would like to give especial thank to Duncan Ashby, I am grateful to be able to work with him in his project, and the methods and tools he taught me about how to do research would benefit me forever.

I would like to give special thanks to Dr. Liu. He advised and inspired me every time I had trouble with my simulation.

Finally, I would like to thank my parents, they are the biggest supporter for me in my life. Although there were 15-hour time difference between me and them, they would comfort and enlighten me whenever I felt upset or lonely.

ABSTRACT OF THE THESIS

Simulation of a Photocatalytic Microreactor with COMSOL Multiphysics

by

Kairui Xia

Master of Science, Graduate Program in Mechanical Engineering
University of California, Riverside, September 2018
Dr. Masaru Rao, Chairperson

Producing enough drinkable water for long-term deep space missions is a great challenge. A small scale photocatalytic microreactor with nano-porous TiO_2 coated titanium micropillar arrays is designed to solve the problem. The COMSOL Multiphysics is used to simulate several parts of the microreactor. The first objective is to model the tree-branched bifurcating flow distribution design and the diamond-shaped flow distribution design, then subsequently compare the pressure drop between the two. Based on simulation results, the tree-branched bifurcating flow distribution design can provide a longer residence time for the waste liquid due to the lower pressure drop inside the distribution channels which increases the photocatalytic efficiency. However, the extension of channels increases the area that this design takes up, thus reducing the size of the reactor chamber. The diamond-shaped distributor is more compact in size because of its geometry which gives more space to the reactor chamber. However, the pressure drop in the microreactor increases about 256% compared to the pressure drop of tree-branched bifurcating distributor which reduces the residence time. The second objective is to simulate photon

interaction among micropillars and light intensity along the micropillars under UV irradiation, then find how the micropillar height influences the light intensity on the micropillar. According to simulation, light intensity on the 50 μm height micropillar creates an ideal photocatalytic efficiency. For the 100 μm height micropillar, 50% of the micropillar has low light intensity which causes low photocatalytic efficiency. And 66.67% of the 150 μm height micropillar's surface has low light intensity. As the height of the micropillar increases, a larger percentage of the micropillar's surface will have low light intensity. This leads to a decrease in photocatalytic efficiency.

TABLE OF CONTENTS

LIST OF FIGURES

LIST OF TABLES

1. Introduction

1.1 Motivation

70% of the Earth's surface is covered by water, only 2.5% of it is fresh and drinkable. Research shows that this limited resource of water will need to support a population of approximately 9.7 billion in 2050 (Guppy & Anderson, 2017). What makes the situation worse is water pollution, according to the Water.org, 1 in 9 people does not have the access to safe and purified water ("Water Crisis - Learn About The Global Water Crisis | Water.org", 2018). Water pollutions come from lots of places, and there are two main types of pollutants, the disease-causing agents and the industrial wastes. Industrial wastes usually contain asbestos, lead, mercury, oils, etc. For the disease-causing agents, most of them are bacteria and viruses. For some developing countries, building large-scale water decontamination facilities is difficult due to the lack of money and technology. Small scale and less expensive water purification devices are good for helping people in some developing countries purify the water.

Producing purified drinkable water is also a big challenge for the international space station (ISS) ("Water on the Space Station | Science Mission Directorate", 2018). Storing drinkable water in the ISS for a long period of time is challenging due to its volume and cost, recycling used water is the best choice to get purified water (NASA, 2000). The technology used now on the ISS is the Water Processor Assembly (WPA), the elimination of volatile organic compound is fulfilled by an oxidization catalytic reactor using high temperature and pressure (John Steele, Mark Wilson, Janice Makinen, 2018). However, the challenge with this device is that the high operation temperature and pressure cause

frequent exchange of vulnerable parts. For overcoming these challenges, a new photocatalytic water purification microreactor which operates under standard temperature and pressure is designed. This paper talks about using COMSOL Multiphysics to simulate two different shaped flow distributors and photon interaction with micropillars of the microreactor. This simulation saves time and material, the result can be used to compare the pressure drop within two flow distributors as well as investigate the photon interaction with micropillars.

1.2 Objectives

This project concentrates on developing simulations using COMSOL Multiphysics and has two objectives. The first is to model the tree-branched bifurcating flow distributor and the diamond-shaped flow distributor, then the pressure drop and water flow in these two flow distributors are compared. The second objective is to simulate photon interaction with micropillars and find light intensity along the micropillars under UV irradiation, then understand how the micropillar height influences the light intensity along the micropillar.

For our lab's microreactor, two significant factors which affect the efficiency of this microreactor are the flow distribution design and the heights of the micropillars. The flow distributor influences the throughput of the microreactor, and the heights of micropillars decide how deep active photons can penetrate. There are two types of flow distributors, the tree-branched flow distributor and the diamond-shaped flow distributor. For finding the advantage and disadvantage of these two distributors, COMSOL

Multiphysics is used to develop simulations, the pressure drop within two flow distributors would be gathered and compared.

The second objective is to find photon interaction with micropillars and how the micropillar heights influence the light intensity along the micropillar. Photons are absorbed when they have contact with TiO_2 which results in the reduction of the number of active photons, this reduction leads to the decrease in photocatalytic degradation rate (Egerton, 2014). The absorption of photons also limits the depth to which photons can penetrate. The light intensity on the lower part of micropillars will decrease when less active photons penetrate to that area which leads to a reduction of the photocatalytic degradation rate. Simulating photon interaction with TiO_2 micropillars can help find how micropillar heights influence the light intensity along the pillar. The COMSOL Multiphysics 5.2 is used to develop all the simulations.

2. Literature Review and Theory

2.1 Principles of Photocatalysis

Photocatalysis is a light induced reaction for which the presence of catalyst accelerates the photoreaction. The studies on using photocatalysis with TiO_2 to treat organic impurities in water began about three decades ago (Matthews, 1987). Figure 1 illustrates the mechanism of photocatalysis.

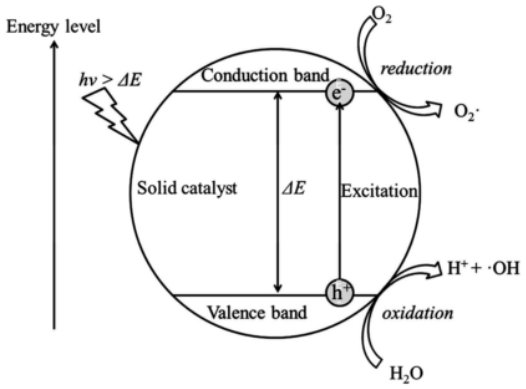

Figure 1: Mechanism of photocatalytic reaction (Xu, Rangaiah, & Zhao, 2014).

TiO_2 semiconductor is taken as an example, the electron will become excited and jump to the conduction band from the valence band when a photon (hv) with energy higher than the band gap (ΔE) of the semiconductor hits the semiconductor. This movement leads to a positively charged hole in the valence band. This movement can be described in equation 1 (C. H. Wu & Chang, 2006):

$$TiO_2 + hv \rightarrow h_{VB}^{+} + e_{CB}^{-} \quad (1)$$

In this equation, hv is the photon, h_{VB}^{+} is the positive charged hole in the valence band, e_{CB}^{-} is the electron which excites in the conduction band. Recombination may happen during the photocatalysis process, the excited electron loses the energy, goes back to the valence band and recombines the hole. Apart from recombination, some reactions as described in equation 2 and equation 3 can occur (C. H. Wu & Chang, 2006):

$$h_{VB}^{+} + H_2O \rightarrow H^{+} + \cdot OH \quad (2)$$

$$e_{CB}^{-} + O_2 \rightarrow \cdot O_2^{-} \quad (3)$$

In equation 2, the water molecules are oxidized by positively charged hole, the hyper-reactive hydroxyl free radicals ($\cdot OH$) is formed. In equation 3, the electron can react with the oxygen to form the oxygen radical ($\cdot O_2^-$). These electrons and excited oxygen species lead to the degradation of microorganic pollutants (Zhao, Chen, & Ma, 2005).

2.2 Titanium Dioxide

Titanium dioxide (TiO_2) is the naturally occurring oxide of titanium. TiO_2 was discovered in 1821 and it was used to replace the toxic lead oxides as pigments for white paint in the beginning of 20th century ("Pigments through the Ages - History - Titanium Dioxide Whites", 2018). As technology develops, it is used as pigments in lots of areas such as paints, plastic, paper, and leather. TiO_2 is also approved as food coloring under the EU legislation on safety of food additives (Carp, Huisman, & Reller, 2004). Due to its high refractive index, TiO_2 is used as anti-reflection coating in many devices and it is also used in the sunscreen cream (Jacobs, van de Poel, & Osseweijer, 2010).

Since photocatalysis with TiO_2 has been a very popular research subject in recent years, it has been used in many application areas such as water purification systems, hydrogen evolution, sterilization and self-cleaning surfaces (Nakata & Fujishima, 2012). The catalyst is one of the most important issue for photocatalysis and various of materials can be used such as TiO_2, ZnO, CeO_2, ZrO_2, etc. TiO_2 is the most widely studied and used photocatalyst material (Ren, Koshy, Chen, Qi, & Sorrell, 2017). The relatively low price and the non-toxic property are the main reasons why TiO_2 is widely used (Skocaj, Filipic, Petkovic, & Novak, 2011). TiO_2 has highly stable chemical and mechanical characteristic

which makes it perfect to be the catalyst (Hamad, Catlow, Woodley, Lago, & Mejías, 2005). On an illuminated surface, TiO_2 can provide the UV-induced superhydrophilicity which makes the water contact angle can approach 0°. This property is applied to some areas such as anti-fogging and self-cleaning process (Fujishima, Zhang, & Tryk, 2007; R. Wang & Hashimoto, n.d.).

The TiO_2 photocatalysts have several different structural design such as spheres, fibers, channels and nanosheets (Nakata & Fujishima, 2012). The most widely studied and used TiO2 photocatalyst is the Degussa P25 which is a TiO_2 nanoparticles powder. These nanoparticles can provide high specific area and high pore volume which benefits the photocatalytic degradation. However, the nanoscale size makes filtration be needed for removing TiO_2 nanoparticles from purified water which makes the process more time-consuming. The nano-porous TiO_2 has the potential to overcome these drawbacks, and it can provide high surface-to-volume ratio as well as good fluid accessibility owing to its 3D porous structure.

2.3 Nano-porous Titanium Dioxide

The photocatalysis has been proven to be one of the most efficient methods for degrading organic pollutants in waste water (Fujishima, Rao, & Tryk, 2000; Gaya & Abdullah, 2008; Herrmann, 1999). Slurry and immobilized are two major types of photocatalytic reactors. In the slurry photoreactor, the photocatalyst is mixed with the solution. Filtration is needed after the photoreaction for separating photocatalyst nanoparticles and purified water. Filtering nanoparticles is a time-consuming process and

the complexity of design for slurry reactors is added. The slurry reactor is not good for the continuous flow system (Sakkas et al., 2004). In the immobilized reactor, thin-film photocatalyst is utilized to accomplish the photoreaction. One advantage is that the thin-film TiO_2 is easily adopted and configured to continuous flow system. Another advantage is that the immobilized reactor does not have any particle aggregation. However, the photocatalytic efficiency of the immobilized reactor is lower than the slurry reactor due to the photocatalyst in slurry reactor having larger reaction area.

For finding a better solution, the nano-porous TiO_2 (NPT) could be used. Hydrogen peroxide solutions are used to oxidize the titanium, and the NPT is grown directly from the titanium substrate which makes the adhesion between NPT and titanium substrate strong (J. M. Wu, 2004). Meanwhile, M. DeRosa et al. found that oxidation of patterned thin titanium films in aqueous hydrogen peroxide can fabricate crack-free NPT (DeRosa, Zuruzi, & MacDonald, 2006). NPT fabricated by using hydrogen peroxide solutions shows some advantages of large surface area, good scalability and fine fluid accessibility. The higher surface-to-volume ratio compared with flat thin-film TiO_2 increases the organic degradation efficiency.

Research shows that NPT can be used in a variety number of applications. A. S. Zuruzi et al. found the nanostructured TiO_2 fabricated by directly oxidizing titanium films in aqueous hydrogen peroxide solution has the potential to be used as a vehicle for gene therapy, and it could also be applied to areas such as energy conversion, separation, photocatalysis and gas sensing (Zuruzi & MacDonald, 2005). Song et al. researched using TiO_2 thin-films with various nanostructures of quasi-aligned nanorods and nanochannels

to photodegrade three different dyes in water under UV illumination and compared the result to only using the thin-film TiO_2. Results showed that the thin-film TiO_2 with nanostructure TiO_2 on the top had better degradation efficiency (Song, Wu, & Yan, 2009). Researches demonstrate the NPT's potential for photocatalytic water purification which makes NPT an ideal material for use in the microreactor.

2.4 Photocatalytic Microreactors

Photocatalytic microreactors are very promising devices where photocatalytic reactions can take place. However, the flurry reactors and immobilized reactors both show some disadvantages such as low mass transfer rate, low photon transfer efficiency and deficiency of dissolved oxygen. The microfluidic microreactor was found to have many advantages over the traditional flurry and immobilized reactors. The photocatalysis could be benefit from large surface area, short diffusion length, uniform residence time, uniform irradiation as well as the easy-controllable operating conditions (N. Wang, Zhang, Wang, Yu, & Chan, 2014). Lots of research shows many photocatalytic microreactors with different geometries.

The work by L. Li et al. presented an optofluidic microreactor with the TiO_2-coated fiberglass immersed in the microreactor chamber. At first, the TiO_2 was coated onto the surface of the fiberglass. The coated fiberglass was loaded into the microreactor after the first step. The tree-branched bifurcating distributors were placed at two sides of the microreactor, and the reactants flowed in through the distributor and had contact with the photocatalyst coated on the fiberglass during the working process. The 2×10^{-5} M

methylene blue solution was used as the reactant. As a result, this microreactor had 40% maximal increment of the degradation efficiency than the normal microreactor where TiO_2 was coated on walls of the microreactor chamber (Li et al., 2013). The good points of this design of microreactor were reducing the transport length and induction of perturbation to the liquid flow. The drawback was the real reaction surface was not large enough. After one year, L. Li's group reported another photocatalytic microreactor with micropillars arrays in the microreactor chamber. This microreactor was made of polydimethylsiloxane (PDMS) and the micropillars were made of SU-8 functioning as the substrate for the catalyst Pt/TiO_2. Figure 2 shows the geometry of this microreactor.

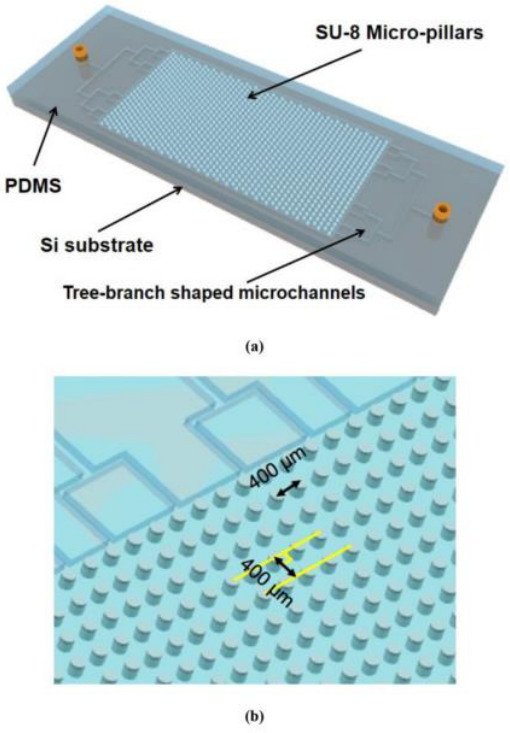

Figure 2: (a) Schematic of the microreactor. (b) Cross section of the reactor chamber (Li et al., 2014).

The catalyst was directly sprayed onto the substrate and the target reactant was 80 mM iodine solution due to photoreaction being used to do water splitting in the project. The flow distributors were still tree-branched-shaped. The result of this experiment showed that the maximal increment of reaction rate could reach 56% compared to the normal planar microreactor (Li et al., 2014). Compared with the microreactor they made in 2013, the surface area of photocatalyst was increased, but the method used to coat the TiO_2 was proved to be problematic which reduced the durability of this microreactor a lot. In 2015, a new microreactor was published by L. Li's group, the geometry of the microreactor was different from the microreactor built in 2014. Instead of using the micropillars arrays, the microgroove was used to enhance the reaction area, these microgrooves had 2 cm length, 200 μm width and 180 μm depth, and there were 8 microgrooves in the microreactor chamber. Because of low durability of the 2014 model, the fabricating process changed from directly spraying Pt/TiO_2 onto the substrate to a casting-transfer method which gave the microreactor higher mechanical strength and durability. The result of this experiment showed that this microreactor had higher hydrogen production rate compared to the 2014 model (Chen et al., 2015). Although the durability and mass transport enhanced, the area of surface where photocatalysis happened reduced due to the microgroove structure, the surface-to-volume ratio was lower than the ratio of microreactor with micropillars in it.

More papers report lots of photocatalytic microreactors with different geometries. One group used ultrasonic to fabricate thin film TiO2 inside a fluoropolymer channel (Colmenares, Nair, Kuna, & Łomot, 2018). Another group introduced gas into the microreactor which combined photocatalysis and ozonation (He et al., 2016).

In our project, a microreactor with more intense titanium micropillar arrays is fabricated to provide higher surface-to-volume ratio, NPT is grown on titanium micropillars to produce the better photocatalytic degradation efficiency. COMSOL Multiphysics is used to model this microreactor.

2.5 COMSOL Multiphysics

COMSOL Multiphysics is a commercial general-purpose platform software for engineering modeling ("The COMSOL® Software Product Suite", 2018). It is widely used in optimizing and verifying the real-world devices and processes. The user interface is well arranged which makes it very easy to learn for a new user.

COMSOL Multiphysics has a core package and lots of add-on modules, if the simulation cannot be developed by the core package, these add-on modules can be used to fulfill various fields of simulation such as electromagnetics, structural mechanics, fluid flow, heat transfer and chemical engineering behavior ("The COMSOL® Software Product Suite", 2018). The add-on modules use several methods such as finite element analysis, the finite volume method, the boundary element method and the particle tracing methods.

Lots of research groups used COMSOL Multiphysics to do simulation in a variety of research areas (Cheng, Ji, Zhu, & Shi, 2010; Diaz-Viera, Lopez-Falcon, Moctezµma-Berthier, & Ortiz-Tapia, 2008; Rebiai, Bahouh, & Sahli, 2013). Two microreactor groups used it to examine how convection and diffusion of reactant molecules affected the performance of microreactors (Jayamohan et al., 2015; Yusuf, Garlisi, & Palmisano, 2018).

In this project, the fluid flow module was used for the flow distribution design structure simulation and ray optics module was used for the light intensity simulation.

3. Experimental Photocatalytic Microreactor

3.1 Current Lab Design

The photocatalytic microreactor in this project was formed by three parts which were the reactor chamber, inlet and outlet, and the microreactor cover. Titanium micropillars were fabricated with 20 µm diameter, 40 µm pitch in the microreactor chamber. The micropillars fabricated by this process had two advantages, the smooth sidewalls and high aspect ratio (Parker, Thibeault, Aimi, Rao, & MacDonald, 2005). These micropillars were placed in an offset manner and they were formed into arrays. NPT was oxidized onto titanium micropillars using hydrogen peroxide solutions under a low temperature of 353 K (J. M. Wu, 2004). Figure 3 shows a cut view of the micropillar arrays.

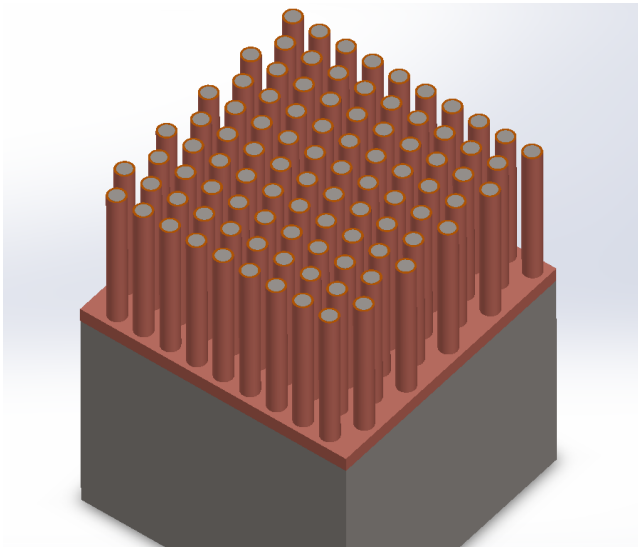

Figure 3: Solidworks model of micropillars cut to show the titanium core.

In figure 3, the substrate and the interior of micropillars which show color in grey are titanium, the exterior of micropillars and the thin layer on substrate which show color in brown are NPT. During the experiment, target liquid would flow through and have contact with the micropillars, UV light would enter from the top of the microreactor. Due to the refraction of water and the angle of light which comes out from the UV lamp, UV light would not go vertically when it transmits in the microreactor among the micropillars. Some photons would be absorbed after having contact with micropillars which decreases the light intensity of UV rays. This phenomenon makes the height of micropillars one of the most influential issues that could influence the efficiency of photocatalysis.

4. Method and Simulation Theory

4.1 Flow Distribution Design Simulation

4.1.1 Experimental Method

In this simulation, the pressure drop and flow velocity magnitude in two different flow distributors were compared. The Laminar Flow interface from the Fluid Flow add-on modules of COMSOL Multiphysics was used. The flow and pressure of liquid and gas could be simulated by using the Fluid Flow module. In this model, water flew through the flow distributor into the reaction chamber, then water flew through all the micropillars into several outlets. Time dependent study was chosen because it could show how flow and pressure changed after a certain time.

These two models were the microreactor with tree-branched bifurcating flow distributor and the microreactor with diamond-shaped flow distributor. The tree-branched

bifurcating flow distributor is commonly used in many microreactors (Azzouz et al., 2018; Li, Tang, Song, & Jiang, 2018; Liao et al., 2016), this distributor has the advantage of low pressure-drop and uniform filling of water. However, the tree-branched bifurcating shape requires larger channel by tiers. In this simulation, the width of channel was decreased by a factor of 1.6 which would lead to gradually slowing down of the flow according to the report (Vangelooven et al., 2010). It makes the tree-branched bifurcating design take up more space on the wafer. For the diamond-shaped distributor, it has an advantage of saving space for reactor chamber in a microreactor. The design of the diamond-shaped bifurcator model in this project was based on figure 4. Studies mostly focused on comparing the flow velocity of two different flow distribution design (Vangelooven et al., 2010). In this project, simulation was used to find the difference of pressure drop.

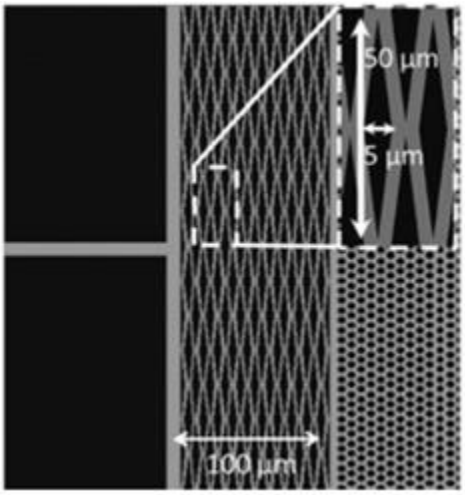

Figure 4: Diamond-shaped distributor model (Vangelooven et al., 2010).

For comparing the two flow distribution design, two COMSOL Multiphysics models were made and the pressure drop was measured.

4.1.2 Assumptions

The models were built under the assumptions listed below. Due to these assumptions, the models differed from theory in terms of:

- UV light was not concerned in the simulation.
- The inlet water flow rate was considered as a constant.
- Any heat exchange was neglected in the simulation.
- Small particles in the water was neglected in the simulation.

4.1.3 COMSOL Multiphysics Model

4.1.3.1 Geometry

The models made in the simulation were smaller than the real microreactor due to simulating the whole microreactor would reach the limitations of the hardware. All simulations were performed at 2D dimension in a top view of the microreactor. The geometry was consisted of the flow distributor, the microreactor chamber, micropillars and outlet channels. Micropillars were placed in an offset manner which could enhance the contact area with water and made the flow slightly slower (Chang, Lee, & Liepmann, 2005). Figures of these models are shown below.

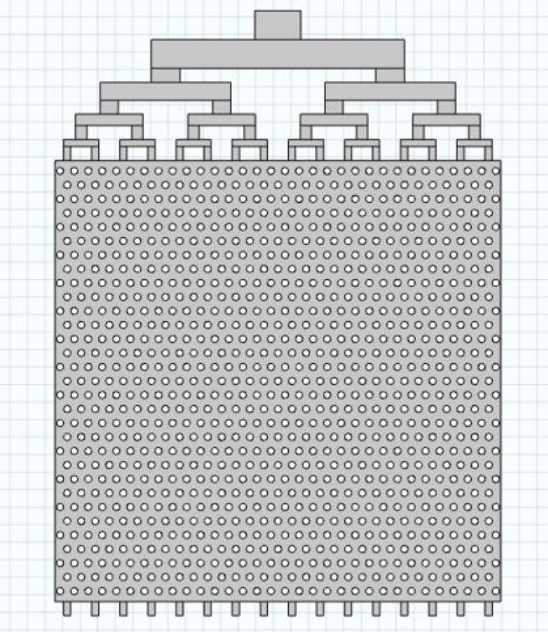

Figure 5: Geometry of tree-branched bifurcating distributor simulation model.

The geometry of tree-branched bifurcating distributor model is shown in figure 5. There were four tiers of branches in the flow distributor. The width of channels which directly connected with the chamber was 20 μm and the distance between these channels was 40 μm. The widths of channels on other tiers were increased by a factor of 1.6 (Vangelooven et al., 2010). In this simulation, the place where micropillars appeared was emptied, these blank circles functioned as micropillars while running the simulation. The boundary conditions of all the walls were set as no-slip. There were 16 outlet channels because the inlet and outlet distribution structure were supposed to be the same. Water flew in from the top of model and flew out from the bottom.

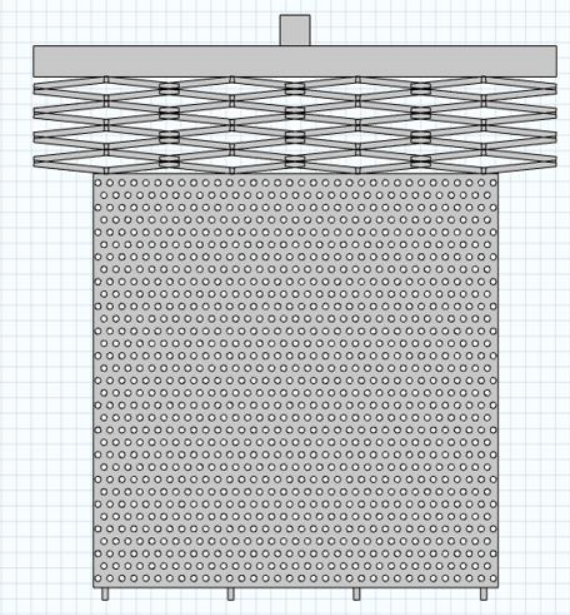

Figure 6: Geometry of diamond-shaped distributor simulation model.

The geometry of diamond-shaped distributor model is shown in figure 6. This distributor model also had four tiers of channels to match the tiers in tree-branched bifurcating distributor model. The width of channels in the distributor was 20 μm. The dimension design of this model was inspired by the dimension in figure 4 (Vangelooven et al., 2010). Assuming the diamond-shaped flow distributor in figure 6 was consisted of lots of rhombuses, each rhombus had the small inner angle of 11.42118° and big inner angle of 168.57882°. In this simulation, the place where micropillars appeared was emptied, these blank circles functioned as micropillars while running the simulation. The size of micropillars were same as the size of micropillars in the tree-branched model. Only 4 outlet channels were built according the number of channels which connected the distributor and reactor chamber.

4.1.3.2 Navier-Stokes Equation

The equations which the Laminar Flow interface of COMSOL Multiphysics uses to calculate the flow velocity and pressure are equation 4 and 5, which are also known as the Navier-Stokers equation.

$$\rho \frac{\partial u}{\partial t} + \rho(u \cdot \nabla)u = \nabla \cdot \left[-pI + \mu(\nabla u + (\nabla u)^T - \frac{2}{3}\mu(\nabla \cdot u)\right] + F \quad (4)$$

$$\rho \nabla \cdot (u) = 0 \quad (5)$$

In these equations, ρ is the density, u is the flow velocity, t is time, ∇ is divergence, p is the pressure, $-pI$ is the volumetric stress, F is ρg which is the body force. Equation 5 is the continuity equation. The left side of equation 4 corresponds to the inertial forces. The $-\nabla pI$ corresponds to the pressure forces. The $\nabla \cdot \left[\mu(\nabla u + (\nabla u)^T - \frac{2}{3}\mu(\nabla \cdot u)\right]$ corresponds to the viscous forces. During simulation, the Navier-Stokes equation is solved using no-slip boundary conditions, and it calculates the pressure and fluid velocity in the model. In this simulation, the density ρ of water and the initial velocity u were provided. The time was set to be 1 second and value of time step was set to be 0.001 s. COMSOL Multiphysics used changing time t to calculate the flow velocity and pressure in every domains of the mesh during every timestep.

4.1.3.3 Parameters Used

The parameters used for tree-branched bifurcating distributor model are listed in the table 1. The distributor channels are described from top to bottom. In table 1, W is width, H is height, D is distance between neighbor micropillars' centers.

Description	**Value**	
W and H of first channel	131.072 µm	81.92 µm
W and H of second channel	721.12 µm	81.92 µm
W and H of third channel	81.92 µm	40 µm
W and H of fourth channel	371.2 µm	51.2 µm
W and H of fifth channel	51.2 µm	40 µm
W and H of sixth channel	192 µm	32 µm
W and H of seventh channel	32 µm	40 µm
W and H of eighth channel	100 µm	20 µm
W and H of ninth channel	20 µm	40 µm
Radius of micropillars	10 µm	
Horizontal D	40 µm	
Vertical D	40 µm	
W and H of outlet channels	20 µm	40 µm
Initial flow velocity	0.0001 m/s	

Table 1: Parameters of tree-branched bifurcating distributor model.

The parameters used for diamond-shaped distributor model are listed in the table 2. The distributor channels are described from top to bottom. In this table, W is width, H is height, L is length, D is distance between micropillars' centers.

Description	Value
W and H of first channel	100 µm 100 µm
W and H of second channel	1746 µm 100 µm
W and L of first oblique channel	20 µm 250 µm
Angle of inclination of first oblique channel	5.71059 deg
Radius of micropillars	10 µm
Horizontal D	40 µm
Vertical D	40 µm
W and H of outlet channels	20 µm 40 µm
Initial flow velocity	0.0001 m/s

Table 2: Parameters of diamond-shaped distributor model.

For both models, the material was set to be water in all the areas. The boundary conditions of all the walls were set to be no-slip. Initial flow velocity was 0.0001 m/s, this value would be changed when the specific value for physical experiment was determined. The time steps for both models were set to be 0.001 second with 1 second total time, which provided 1000 time-elements while running the simulation.

4.2 Light Intensity Simulation

4.2.1 Experimental Method

The objective of this simulation is to find photon interaction among micropillars and how the height of micropillars influences the light intensity along the micropillar. The COMSOL Multiphysics was used to fulfill the target. The Geometrical Optics interface from Ray Optics add-on module was selected. The idea of this simulation was inspired by two COMSOL examples (Comsol, n.d.; Definition, n.d.). Geometrical Optics had the built-

in tools for computing the intensity, phase and optical path length of rays which made it a perfect selection for this simulation. The Ray Tracing Study was selected because it could compute the trajectories of rays which gave us a direct view of how photons moved among the micropillars. In an optical system, ray tracing happens in two steps ("How Does the Choice of Ray Tracing Algorithm Affect the Solution?", 2018):

1. Set an initial ray position and direction, the ray tracing algorithm will trace the movements of rays until they hit the next boundary.

2. When rays hit the boundary, the ray tracing algorithm will adjust the ray direction, such as reflection or refraction, according to the boundary condition. Then this ray will be traced again through the subsequent media by ray tracing algorithm.

At first, a microreactor 2D model was made. However, the 2D model was too limited for simulating the movements of photons because photons could be reflected into different angles while 2D model could only simulate the photon movements in one plane. Then, a 3D microreactor model with 324 micropillars was made. This 3D model showed the complex movements of photons among the micropillars. However, this model had some disadvantages. First, the movements of photons were in a mess and it was hard to extract any data from the simulation results. Second, the number of rays was not large enough compared with the size of the model. In the end, a simplified model was decided to develop the simulation. In this model, only one micropillar was used and the boundary conditions of the surrounding walls were set to be specular reflection. The purpose of this setting was using this one micropillar to simulate a whole micropillar matrix. The theory of this model design is explained in the following geometry section.

4.2.2 Assumptions

The model was built under the assumptions listed below. Due to these assumptions, the model differed from theory in terms of:

- There was no any heat exchange inside the system.
- The small difference of distances between micropillars did not affect the result.
- Surface roughness of the micropillar was not considered.
- Small particles in the water was neglected in the simulation.

4.2.3 COMSOL Multiphysics Model

4.2.3.1 Geometry

The simulation was performed at 3D dimension. The model could be divided into two parts: the first part was the inner cylinder, it functioned as the micropillar while running simulation; the second part was the circular ring outside the small cylinder, it functioned as water while running simulation. Figure 7 shows the geometry of this model.

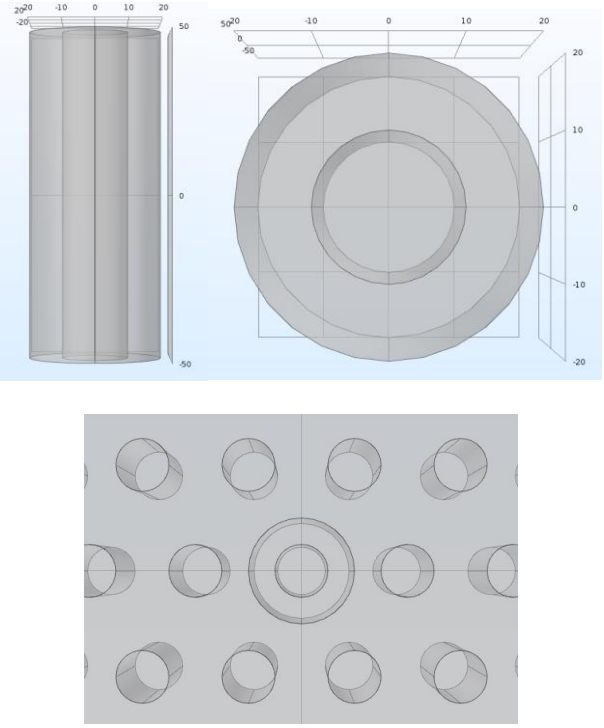

Figure 7: Top left and top right pictures are side view and top view of model; picture below shows the top view of the model in micropillar arrays.

In figure 7, the radius of inner cylinder was 10 μm, and the radius of circular ring was 20 μm. As mentioned above, this one micropillar was used to simulate all the micropillars. The boundary condition of the outboard surface was set to be specular reflection. Without this reflection boundary, photons would go straight and hit a micropillar. However, when the reflection boundary was set, photons would be mirror reflected and hit the only micropillar in the model. The distance between two neighbor micropillars in one row was 40 μm, the radius of cylinder ring was set to be 20 μm so the specular reflection boundary could be set in the middle of two neighbor micropillars. This geometry was used because we tried to have the maximum number of rays in a small model to make the results

more accurate, the hardware ability limited the number of rays which could be used in this simulation. The material of inner cylinder was TiO_2, and material of circular ring was water.

For finding the light intensity on the surface of inner pillar, the intensity computation interface was used. This interface was set to "compute intensity and power". The intensity of each ray was computed along its trajectory which could help us record the light intensity when rays hit surface of the micropillar. The freeze boundary condition was set for the surface of inner cylinder and it allowed light intensity data to be obtained when rays hit that surface. The average light intensity on surface of inner micropillar was calculated every 10 μm in vertical direction. The heights of micropillars were changed for analyzing how micropillars heights influenced light intensity on micropillars.

4.2.3.2 Ray Tracing Equation

COMSOL Multiphysics ray tracing method uses a set coupled first-order ordinary differential equations as equation 5 and 6 to fulfill the function.

$$\frac{dq}{dt} = \frac{d\omega}{dk} \quad (6)$$

$$\frac{dk}{dt} = -\frac{d\omega}{dq} \quad (7)$$

In equation 6 and 7, q is the instantaneous ray position. k is the wave vector which points in the direction in which the wave propagates and it equals to $\frac{2\pi}{\lambda}$ where λ is the wavelength. ω is the angular frequency which equals to $\frac{2\pi}{T}$. The speed of wave travels in one direction equals to $\frac{\lambda}{T}$ which can be represented by $\frac{\omega}{k}$. When rays transmit in one media, $\frac{dk}{dt} = 0$ and it keeps the speed and direction of rays. When rays have contact with another

media, COMSOL Multiphysics computes the direction of the refracted rays using Snell's law. The initial ray position and the initial ray direction were known, time was set to be 1 ns with 8500 time steps. The ray tracing algorithm used changing time to decide the position and direction of rays. This is also a time-dependent study, the rays at different instances of time are shown in the results.

4.2.3.3 Parameters Used

Some numerical parameters are listed in table 3. In this table, R is radius, H is height.

Description	**Value**
R of inner cylinder	10 μm
R of circular ring	20 μm
H of cylinder and ring	50, 100, 150 μm
Total source power	6.10726×10^{-7} W
Inlet light angle	π/12.94 rad

Table 3: Parameters used in light intensity simulation.

The reason why height was chosen for 50, 100, 150 μm was because simulations on 200, 300, 400 and 500 μm micropillars were done and it showed that the light intensity along the pillar was too low compared with the data from studies of the relationship between light intensity and photocatalytic efficiency (Benabbou, Derriche, Felix, Lejeune, & Guillard, 2007; Pansamut, Charinpanitkul, & Suriyawong, 2013). The low light intensity If a large part of the micropillar's surface had low light intensity, the photocatalytic

efficiency could be reduced. Therefore, the final simulation focused on micropillars with heights of 50, 100, 150 μm.

The total source power of inlet light source was calculated by using light intensity of UV lamp multiplying the top area of the model. The light intensity of UV lamp was 486 W/m^2 with 365 nm wavelength and the area of top surface was 400 π μm^2. After calculation, the total source power of light which illuminated the model was 6.10726 x 10^{-7} W.

The total number of rays was 15000. There were 150 point light source points in total, and each point had 100 rays sent out. These 150 light source points were arranged uniformly on the top of model except the inner cylinder's top area. The left picture in figure 8 shows how light sources were arranged on the top of model. The largest number of rays that could be chosen was 15000, which was limited by the hardware ability.

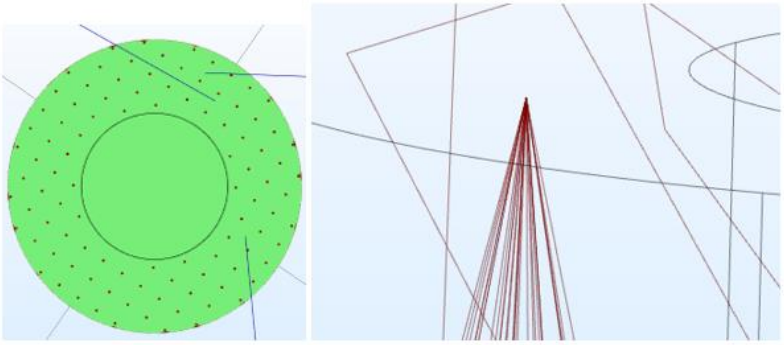

Figure 8: Left picture shows top view of model with 100 light source points; right picture shows rays released from one light source point with light angles.

The cone inlet light angle was measured manually. A paper was placed under the UV lamp, and a circle was drawn along the edge of light spot on the paper. Combined with

the distance between UV lamp and paper, the cone light angle was calculated using the Pythagorean theorem and it was π/12.94 rad. All the rays were set with a cone light angle. The right picture in figure 8 shows how light was sent out from one light source point in the simulation.

The value of time step was set to be 1.17647×10^{-4} ns, and the total time was 1 ns. The time was chosen because the light speed was 2.25×10^{8} m/s in water and the size of this model was small, 1 ns was long enough for all the rays propagated inside the microreactor. This time step provided 8500 time-elements during simulation. A study was made by measuring transmission probability while the number of time-step elements was changing to find which value of time-step to choose. Figure 9 shows the result of the study.

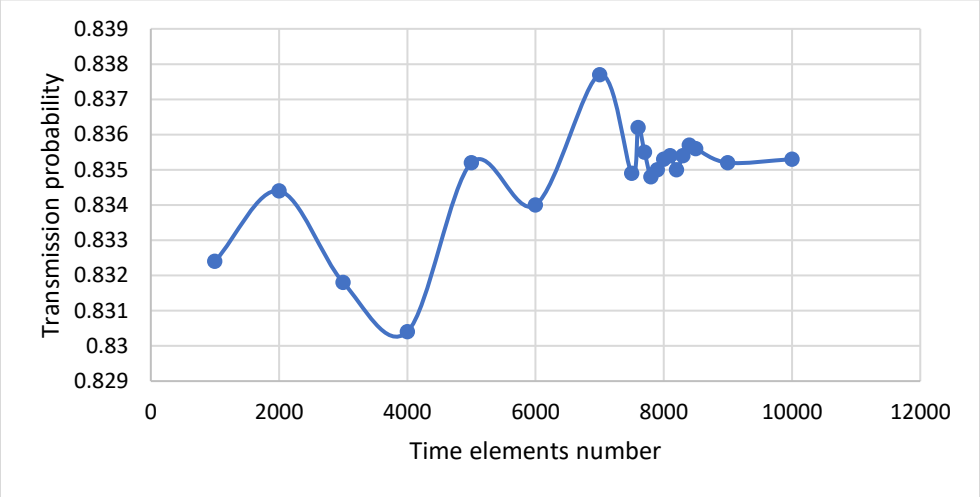

Figure 9: Result of time elements number study.

Elements number	7500	7600	7700	7800	7900	8000
Transmission probability	0.8349	0.8362	0.8355	0.8348	0.835	0.8353
Elements number	8100	8200	8300	8400	8500	
Transmission probability	0.8354	0.835	0.8354	0.8357	0.8356	

Table 4: Change of transmission probability between 7500 and 8500 time elements.

The transmission probability was calculated by using the number of rays hit the model's bottom dividing the total number of rays. Figure 8 showed that after 8500 elements, this curve almost went to flat, and table 4 showed the change of transmission probability from 7500 elements to 8500 elements. It showed that the transmission probability difference between adjacent time-step numbers became small after 8000 elements. Therefore, 8500 time-elements and time step with a value of 1.17647×10^{-4} ns were chosen.

Because the bottom of model was also NPT, the boundary condition on the bottom was set to be diffuse scattering with absorption coefficient of 0.00172. The absorption coefficient of thin-film materials could be calculated by equation 7 (Ilican, Caglar, & Caglar, 2007):

$$\alpha = 2.303 \cdot \frac{Absorbance}{Thickness} \tag{8}$$

In this equation, α was absorption coefficient, absorbance and thickness were provided by an experiment, the absorbance of 1600 nm thick NPT under 365 nm UV light was 1.196 A. After calculation, the absorption coefficient of NPT was 0.00172. The surface of the inner cylinder was set to be freeze, when rays hit it the light intensity data stored in rays would be obtained. The boundary condition of circular ring's wall was set to be specular reflection with a reflection coefficient of 1.

The material of circular ring was set to be water. For the inner cylinder, material was set to be crystal TiO_2 Devore-e.

5. Results and Discussion

5.1 Flow Distribution Design Simulation

5.1.1 Simulation Results

Figure 10 and figure 11 show the velocity magnitude and pressure of tree-branched bifurcating distributor model. Figure 12 and figure 13 show the velocity magnitude and pressure of diamond-shaped distributor model. All these plots showed the result at 1 s which was the final moment of the simulation. In the velocity magnitude figures, the color legend on the right illustrated the flow velocity in m/s. In the pressure figures, the color legend on the right illustrated the pressure in Pa, and the contours across the chamber showed the pressure, the value of pressure remained same on each individual contour.

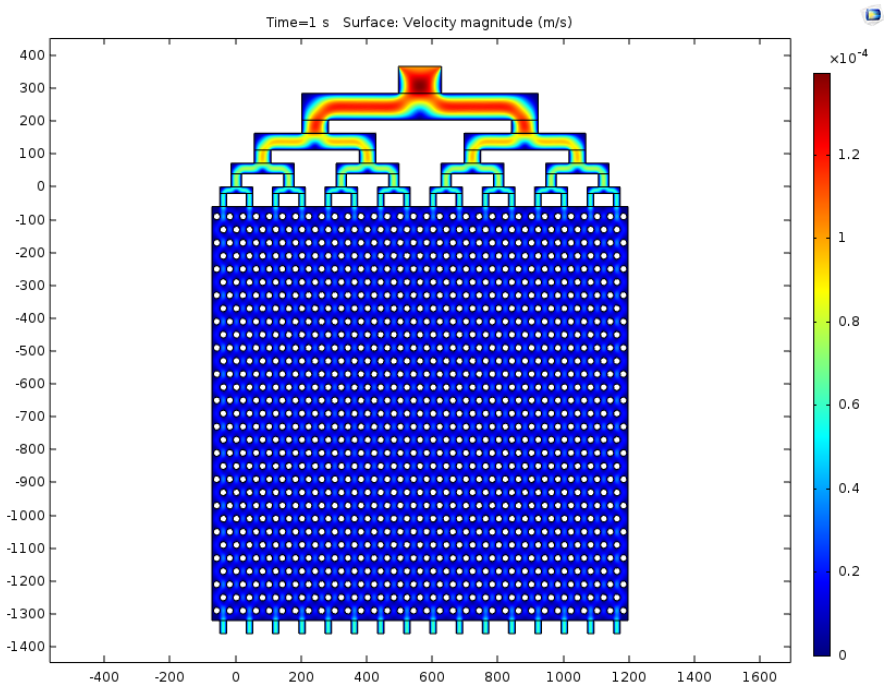

Figure 10: Velocity magnitude plot of tree-branched bifurcating distributor model.

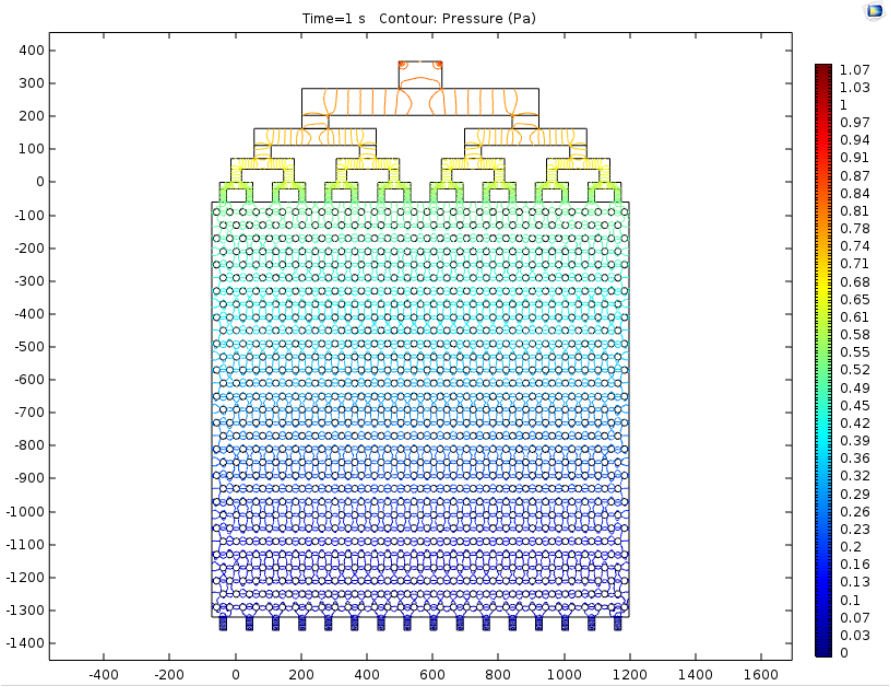

Figure 11: Pressure plot of tree-branched bifurcating distributor model.

In figure 10, for tree-branched bifurcating distributor model, the flow velocity at the inlet was approximately 1.39×10^{-4} m/s and the flow velocity was approximately 0.56×10^{-4} m/s at the fourth-tier flow distributor channel. The changing color of flow velocity in figure 10 also illustrated that the flow velocity decreased uniformly as water ran through the flow distributor. In figure 11, it could be concluded from the color gradient that the pressure kept dropping uniformly while water flew from inlet to outlet, the pressure drop between the inlet and fourth-tier distributor channel was approximately 0.52 Pa, and the pressure drop between the inlet and outlet channels was approximately 1.04 Pa.

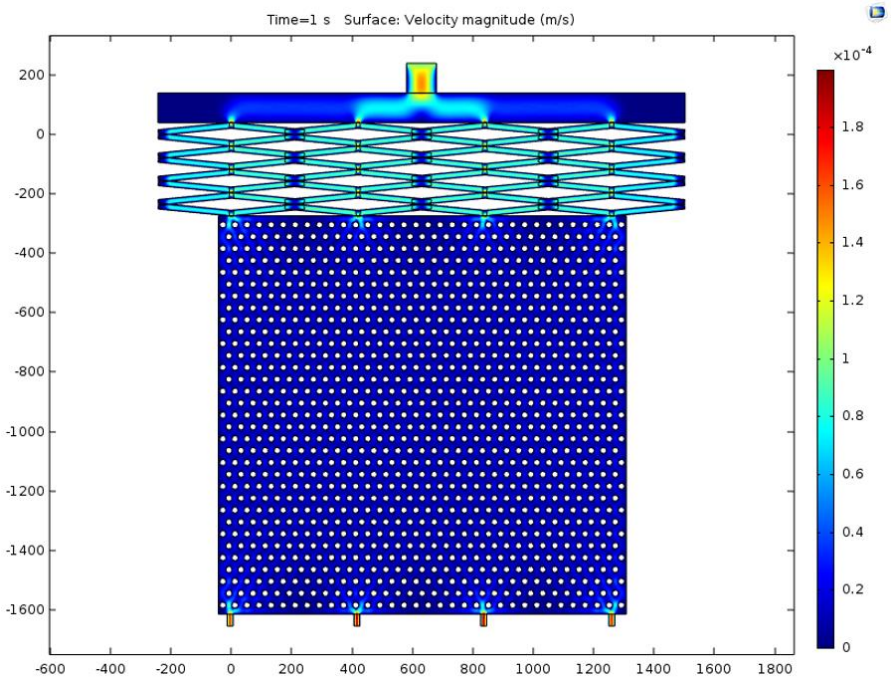

Figure 12: Velocity magnitude plot of diamond-shaped distributor model.

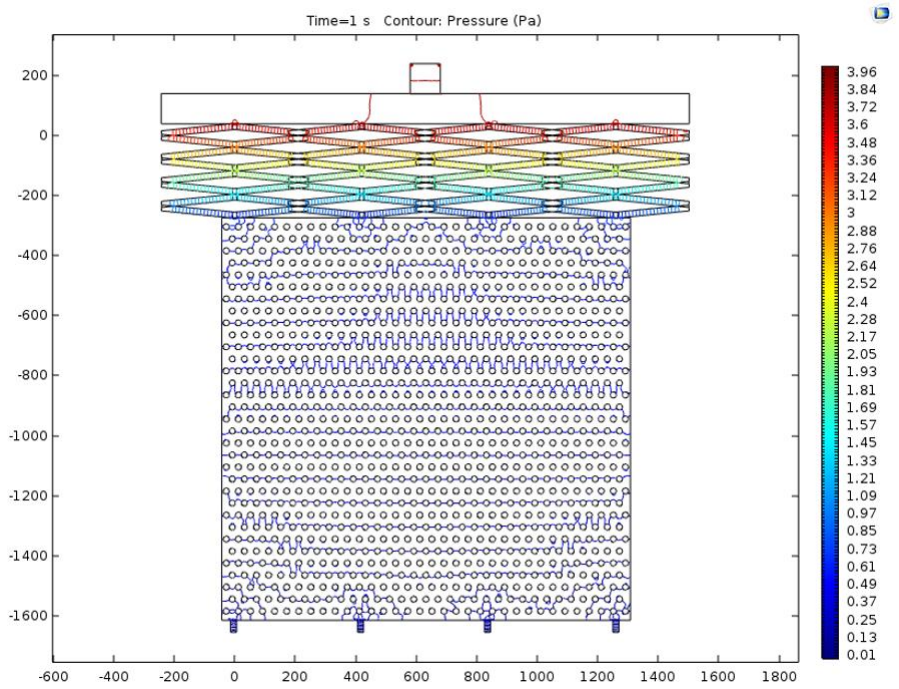

Figure 13: Pressure plot of diamond-shaped distributor model.

Figure 12 reveals that for the diamond-shaped distributor model, the flow velocity at the inlet was approximately 1.47×10^{-4} m/s. While water flew inside the flow distributor the flow velocity remained at approximately 0.9×10^{-4} m/s. The color of flow velocity in figure 12 also illustrated that the flow velocity in the diamond-shaped distributor channel did not have a dramatic change. In the figure 13, the pressure dropped dramatically inside the diamond-shaped distributor channels. The pressure drop between the inlet and fourth-tier channel was approximately 3.47 Pa, and the pressure drop was approximately 3.71 Pa between the inlet and outlet channels.

5.1.2 Comparison of Two Flow Distribution Design

Table 5 shows the parameters obtained from the result of simulation. V_1 is the highest flow velocity at the inlet. V_2 is the highest velocity at the fourth-tier flow distributor channel. V_3 is the approximate average flow velocity in the reactor chamber. P_{drop1} is the pressure drop between the inlet channel and the fourth-tier distributor channel. P_{drop2} is the pressure drop between the inlet channel and the outlet channel.

Symbol	**Value of tree-branched bifurcating model**	**Value of diamond-shaped model**
V_1	1.390×10^{-4} m/s	1.470×10^{-4} m/s
V_2	0.560×10^{-4} m/s	1.130×10^{-4} m/s
V_3	0.164×10^{-4} m/s	0.201×10^{-4} m/s
P_{drop1}	0.52 Pa	3.47 Pa
P_{drop2}	1.04 Pa	3.71 Pa

Table 5: Parameters comparison between two distributor models.

With all the result figures and table 5, it could be concluded that the advantage of tree-branched bifurcating distributor is that it can produce lower pressure drop compared with the pressure drop in the diamond-shaped distributor. According to the value of P_{drop2} from table 5, the pressure drop in the diamond-shaped distributor model increased about 256% compare to the pressure drop in tree-branched bifurcating distributor model. Study showed that pressure drop in a fluid flow system was caused by the resistance of flow, and lower pressure drop resulted in longer residence time (Billet, 1988). The rough residence time of water in the reactor chamber can be calculated by using the V_3 from table 5 as well

as the area of the reactor chamber. The approximate residence time is 76.83 s. For the diamond-shaped distributor, the approximate residence time is 66.67s. The increasing residence time for target liquid in the tree-branched bifurcating distributor can enhance the photocatalytic efficiency. However, the tree-branched bifurcating distributor usually takes up more space than the diamond-shaped distributor on a wafer because of the extension of its channels (Vangelooven et al., 2010). The reactor chamber's size is reduced because of the larger distributor's size.

The diamond-shaped distributor has the advantage of the compact size. It takes up less space on the wafer compared to the space taken by the tree-branched bifurcating distributor. More micropillars could be fabricated due to the larger size of reactor chamber which results in higher photocatalytic efficiency. However, the disadvantage of this flow distribution design is that the larger pressure drop leads to a decrease in residence time which decreases the photocatalytic efficiency.

A basic comparison of these two types of flow distribution designs is presented, which design should be chosen depends on the applicants.

5.2 Light Intensity Simulation

5.2.1 Simulation Results

All the figures show the result at 1 ns which was the final moment for simulation. Take the 50 μm height micropillar model as an example, figure 14 shows what the result looks like.

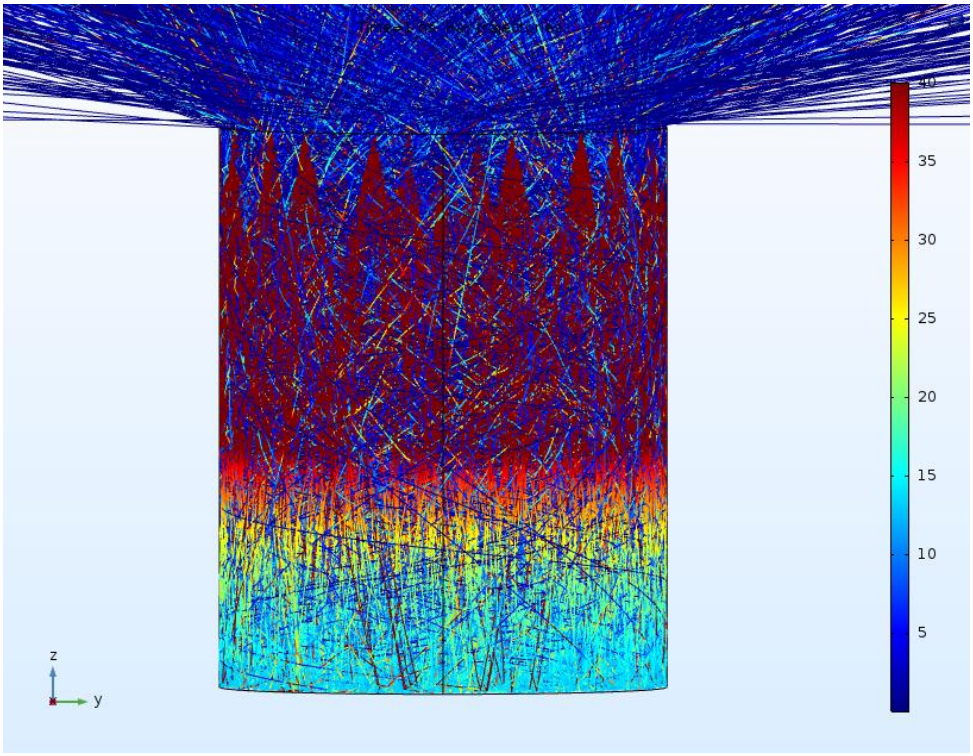

Figure 14: Simulation result with ray traces of the 50 µm height micropillar model.

In figure 14, all the colored lines showed the traces of 15000 rays. The color legend on the right illustrated light intensity of rays in w/m^2. This figure showed that the color of rays changed from red to blue as they propagated in the model which meant that the rays kept losing light intensity. Figure 15 shows the result where all the ray traces were set to be invisible.

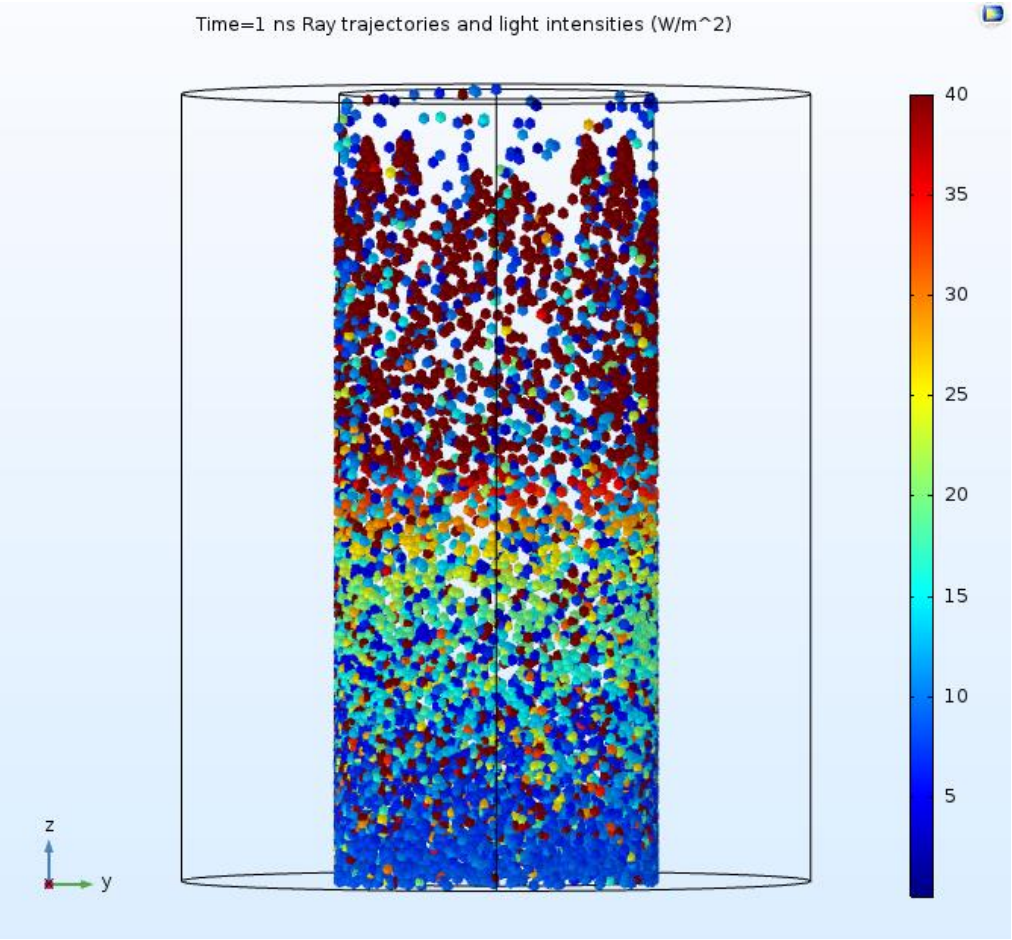

Figure15: Simulation result without ray traces of the 50 µm height micropillar model.

In figure 15, all the small spheres on the surface of inner cylinder exhibited the light intensity when rays had contact with the surface. The color of these spheres represented the value of light intensity. For finding the average light intensity along the micropillars, several planes were made every 10 µm on the micropillar. the light intensities of all small colored spheres on each plane were recorded, then calculation was made to find the average light intensity on each height. This procedure was done on 50 µm, 100 µm and 150 µm micropillar models. Figure 16 shows the result.

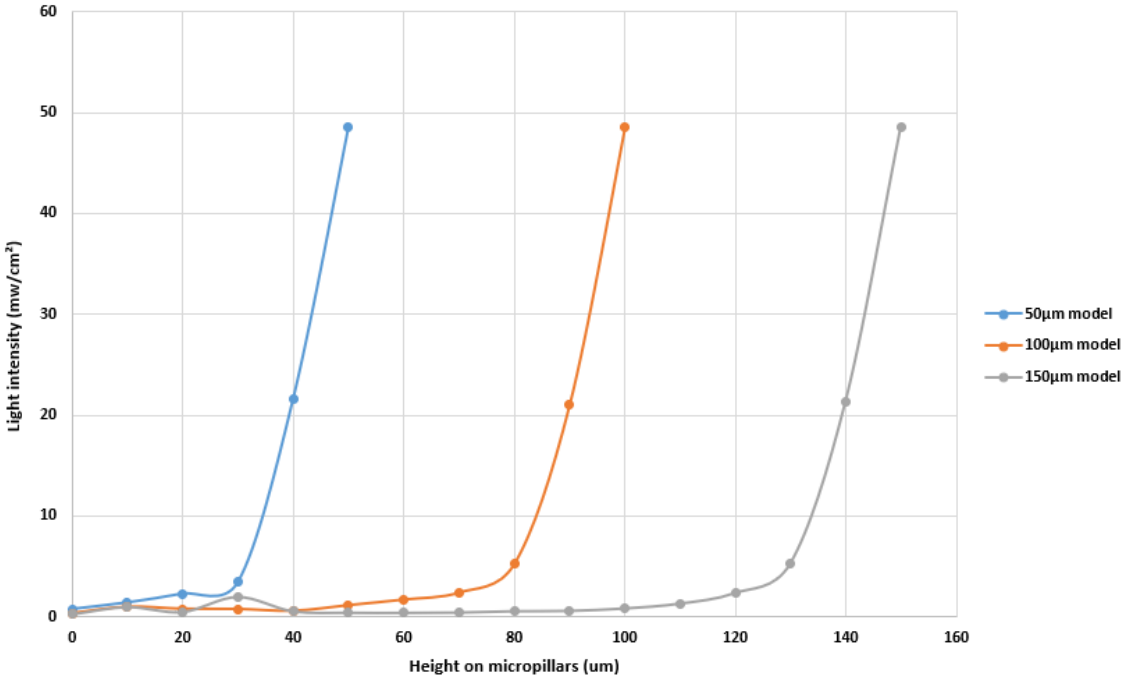

Figure 16: Relationship between light intensity and heights on 50 µm, 100 µm, 150 µm micropillars.

In figure 16, the vertical axis represented the value of average light intensity. The horizontal axis showed the distance between bottom and target planes on the model. Table 6 shows the average light intensity value. In table 6, the first and fifth rows were height points on the micropillar. The first column represented three micropillar models with

different heights. Other cells in the table showed the value of average light intensity with mw/cm^2 as the unit.

	0	10	20	30	40	50	60	70
50um	0.772706	1.420705	2.299339	3.445022	21.65843	48.6		
100um	0.323052	0.962654	0.758742	0.740579	0.558566	1.11902	1.667414	2.36758
150um	0.255567	0.981901	0.489213	1.987431	0.561325	0.421135	0.410883	0.442261
	80	90	100	110	120	130	140	150
50um								
100um	5.2389	21.0723	48.6					
150um	0.574777	0.608303	0.849433	1.328529	2.382371	5.299929	21.37343	48.6

Table 6: Average light intensity along different height micropillars.

5.2.2 Influence of Micropillar Heights

There has been limited research conducted on the influence of light intensity. However, we found a paper written by A.K. Benabbou et al. that details an experiment to see how UV light intensity affects the photocatalytic degradation of Esherishia coli (Benabbou et al., 2007). We decided to use the findings of this paper as a threshold with which to compare our own results. The photocatalyst chosen in A.K. Benabbou's experiment was Degussa P25 TiO_2 and UV light was produced by an HPK 125 lamp. During the experiment, TiO_2 nanoparticles with an average diameter of 20 to 30 nm were mixed with E. coli in the solution, several experiments were conducted with different UV light intensity by using different size of light grids. Figure 17 shows the result of intensity effect on E. coli inactivation.

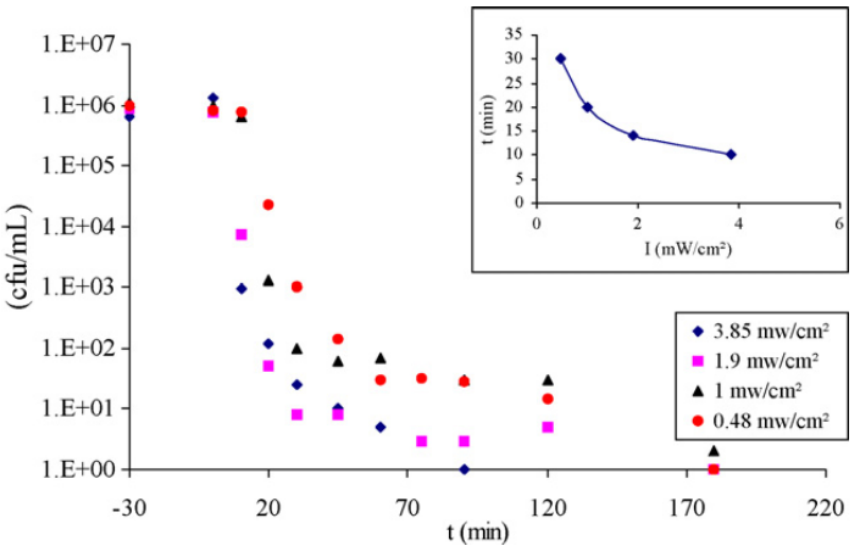

Figure 17: Intensity effect on E. coli inactivation in the UVA domain at TiO_2 concentration of 0.25 g/IL. Insert: time needed to decrease the bacteria concentration from 10^6 to 10^3 cfu/mL as a function of irradiation intensity (Benabbou et al., 2007).

Figure 17 clearly shows that the inactivation rate of E. coli went up as light intensity increased, and light intensity of 3.85 mw/cm^2 led to the highest inactivation efficiency. They found that the increasing of light intensity reduced the time needed for killing bacteria, as shown in the inserted plot in Figure 17. In this paper, they reported that light intensity was an important factor which influences to the photocatalytic degradation efficiency, and higher light intensity led to higher photocatalytic rates. Figure 17 showed that 2 mw/cm^2 was an important divide; when light intensity was higher than 2 mw/cm^2, the increasing of photocatalytic rate would gradually increase. When light intensity was lower than 2 mw/cm^2, a small increase in light intensity would lead to a dramatic increase in photocatalytic rate. While the results of A.K. Benabbou's experiment may be inconclusive, we elected to use the value of 2 mw/cm^2 for the sake of our discussion.

From the result of Benabbou's study, we assumed that if light intensity was much lower than 2 mw/cm^2, the photocatalytic degradation efficiency would be low; if the light intensity was close to or higher than 2 mw/cm^2, the photocatalytic degradation efficiency would be ideal.

In our simulation, for the 150 μm micropillar, the light intensity between the bottom and 100 μm height on the micropillar was around 0.69 mw/cm^2 on average which was much lower than 2 mw/cm^2. It meant that 66.67% of the 150 μm micropillar would have low photocatalytic degradation efficiency. The 100 μm micropillar had an average light intensity of approximately 0.67 mw/cm^2 from 0 μm to 50 μm height which made half of the micropillar have a low photocatalytic degradation efficiency. If the micropillar was higher than 100 μm, more than half of the micropillar would have low photocatalytic degradation efficiency. The 50 μm micropillar had the lowest light intensity at its bottom, approximately 0.77 mw/cm^2, and the light intensity kept increasing along the 50 μm micropillar. The light intensity at 10 μm height was approximately 1.42 mw/cm^2 which was close to 2 mw/cm^2, and it reached about 2.30 mw/cm^2 at 20 μm height. Both results demonstrated that the whole 50 μm micropillar had ideal photocatalytic degradation efficiency.

The results of 50 μm, 100 μm and 150 μm model show that the height of a micropillar influences its light intensity. When the height of micropillar increases, more of the surface of the micropillar will have low light intensity. This leads to a decrease in photocatalytic degradation efficiency. Future work is needed to determine the optimal

micropillar height which allows the microreactor to have the highest photocatalytic degradation efficiency.

6 Conclusion

By utilizing the COMSOL Multiphysics simulations, the two objectives of this project were completed. A comparison between the tree-branched bifurcating distribution design and the diamond-shaped distribution design revealed that they both had their own advantages and disadvantages. The tree-branched bifurcating distribution design can provide more residence time due to the lower pressure drop which increases the photocatalytic efficiency, but the extension of channels makes it take up more space than the diamond-shaped distribution design on a wafer. The diamond-shaped distribution design is more compact in size. It also takes up less area in microreactor compared with tree-branched bifurcating distribution design which results in the larger size of reactor chamber. However, the large pressure drop between inlet and outlet decreases the residence time which subsequently reduces the photocatalytic efficiency.

In examining how height influences light intensity on the micropillar, results show that the a larger micropillar height leads to low light intensity on more of the surface. Rays continue losing light intensity as they propagates in the microreactor. For 50 μm micropillars, light intensity is ideal along the entire micropillar. The lower portion of the 100 μm height micropillar has low light intensity which takes up 50% of the micropillar. Approximately 66.67% of the surface of the 150 μm height micropillar has low light

intensity. All of the results show that the higher micropillar causes more of the surface of the micropillar to have low light intensity which leads to a decrease in photocatalytic efficiency.

7 Future Work

These simulations still need some improvements in the future. The simulations provide comparisons of the advantage and disadvantage of each flow distribution design. More simulations need to be developed using different flow velocities. Physical experiments are needed to determine which flow distribution design is better for our microreactor in the future. As for the light intensity simulation, the surface roughness of micropillars still needs to be considered in the simulation, because the surface roughness influences the absorption and refraction of UV light. Further research will provide a more specific model with a rough surface.

8 Bibliography

Azzouz, I., Habba, Y. G., Capochichi-Gnambodoe, M., Marty, F., Vial, J., Leprince-Wang, Y., & Bourouina, T. (2018). Zinc oxide nano-enabled microfluidic reactor for water purification and its applicability to volatile organic compounds. *Microsystems & Nanoengineering*, *4*(March 2017), 17093. https://doi.org/10.1038/micronano.2017.93

Benabbou, A. K., Derriche, Z., Felix, C., Lejeune, P., & Guillard, C. (2007). Photocatalytic inactivation of Escherischia coli Effect of concentration of TiO 2 and microorganism, nature, and intensity of UV irradiation. https://doi.org/10.1016/j.apcatb.2007.05.026

Billet, R. (1988). Relationship between residence time, fluid dynamics and efficiency in countercurrent flow equipment. *Chemical Engineering & Technology*, *11*(1), 139–148. https://doi.org/10.1002/ceat.270110119

Carp, O., Huisman, C. L., & Reller, A. (2004). Photoinduced reactivity of titanium dioxide. *Progress in Solid State Chemistry*, *32*(1–2), 33–177. https://doi.org/10.1016/j.progsolidstchem.2004.08.001

Chang, W. C., Lee, L. P., & Liepmann, D. (2005). Biomimetic technique for adhesion-based collection and separation of cells in a microfluidic channel. *Lab on a Chip*, *5*(1), 64–73. https://doi.org/10.1039/b400455h

Chen, R., Li, L., Zhu, X., Wang, H., Liao, Q., & Zhang, M. X. (2015). Highly-durable optofluidic microreactor for photocatalytic water splitting. *Energy*, *83*, 797–804. https://doi.org/10.1016/j.energy.2015.02.097

Cheng, J., Ji, L., Zhu, Y., & Shi, Y. (2010). Fluid model of inductively coupled plasma etcher based on COMSOL. *Journal of Semiconductors*, *31*(3), 0–6. https://doi.org/10.1088/1674-4926/31/3/032004

Colmenares, J. C., Nair, V., Kuna, E., & Łomot, D. (2018). Development of photocatalyst coated fluoropolymer based microreactor using ultrasound for water remediation. *Ultrasonics Sonochemistry*, *41*(September 2017), 297–302. https://doi.org/10.1016/j.ultsonch.2017.09.053

Comsol. (n.d.). Transparent Light Pipe. Retrieved from https://www.comsol.com/model/download/404701/models.roptics.light_pipe.pdf

Definition, M. (n.d.). Solar Dish Receiver, *2*(1), 1–14.

DeRosa, D. M., Zuruzi, A. S., & MacDonald, N. C. (2006). Formation of Nanostructured Titania: Effect of Thickness on Oxidation Kinetics of Titanium Thin Films in Aqueous Hydrogen Peroxide. *Advanced Engineering Materials*, *8*(1–2), 77–80. https://doi.org/10.1002/adem.200500186

Diaz-Viera, M. A., Lopez-Falcon, D. A., Moctezµma-Berthier, A., & Ortiz-Tapia, A.

(2008). COMSOL Implementation of a Multiphase Fluid Flow Model in Porous Media. *COMSOL Conference 2008*.

Egerton, T. A. (2014). Uv-absorption-the primary process in photocatalysis and some practical consequences. *Molecules*, *19*(11), 18192–18214. https://doi.org/10.3390/molecules191118192

Fujishima, A., Rao, T. N., & Tryk, D. A. (2000). Titanium dioxide photocatalysis. *Journal of Photochemistry and Photobiology C: Photochemistry Reviews*, *1*(1), 1–21. https://doi.org/10.1016/S1389-5567(00)00002-2

Fujishima, A., Zhang, X., & Tryk, D. A. (2007). Heterogeneous photocatalysis: From water photolysis to applications in environmental cleanup. *International Journal of Hydrogen Energy*, *32*(14), 2664–2672. https://doi.org/10.1016/j.ijhydene.2006.09.009

Gaya, U. I., & Abdullah, A. H. (2008). Heterogeneous photocatalytic degradation of organic contaminants over titanium dioxide: A review of fundamentals, progress and problems. *Journal of Photochemistry and Photobiology C: Photochemistry Reviews*, *9*(1), 1–12. https://doi.org/10.1016/j.jphotochemrev.2007.12.003

Guppy, L., & Anderson, K. (2017). Global Water Crisis: the Facts. *United Nations University Institute for Water, Environment and Health, Hamilton, Canada*. Retrieved from http://inweh.unu.edu/wp-content/uploads/2017/11/Global-Water-Crisis-The-Facts.pdf

Hamad, S., Catlow, C. R. A., Woodley, S. M., Lago, S., & Mejías, J. A. (2005). Structure and Stability of Small TiO $_2$ Nanoparticles. *The Journal of Physical Chemistry B*, *109*(33), 15741–15748. https://doi.org/10.1021/jp0521914

He, X., Chen, R., Zhu, X., Liao, Q., An, L., Cheng, X., & Li, L. (2016). Opto fl uidics-Based Membrane Microreactor for Wastewater Treatment by Photocatalytic Ozonation. https://doi.org/10.1021/acs.iecr.6b00562

Herrmann, J. M. (1999). Heterogeneous photocatalysis: Fundamentals and applications to the removal of various types of aqueous pollutants. *Catalysis Today*, *53*(1), 115–129. https://doi.org/10.1016/S0920-5861(99)00107-8

Ilican, S., Caglar, M., & Caglar, Y. (2007). Determination of the thickness and optical constants of transparent indiμm-doped ZnO thin films by the envelope method. *Materials Science-Poland*, *25*(3), 709–718.

Jacobs, J. F., van de Poel, I., & Osseweijer, P. (2010). Sunscreens with Titanium Dioxide (TiO2) Nano-Particles: A Societal Experiment. *NanoEthics*, *4*(2), 103–113. https://doi.org/10.1007/s11569-010-0090-y

Jayamohan, H., Smith, Y. R., Hansen, L. C., Mohanty, S. K., Gale, B. K., & Misra, M. (2015). Anodized titania nanotube array microfluidic device for photocatalytic

application: Experiment and simulation. *Applied Catalysis B: Environmental*, *174–175*, 167–175. https://doi.org/10.1016/j.apcatb.2015.02.041

John Steele, Mark Wilson, Janice Makinen, C. M. O. (2018). Antimicrobials for Water Systems in Manned Spaceflight – Past, Present, and Future Applications and Challenges. *International Conference on Environmental Systems*, (July).

Li, L., Chen, R., Liao, Q., Zhu, X., Wang, G., & Wang, D. (2014). High surface area optofluidic microreactor for redox mediated photocatalytic water splitting. *International Journal of Hydrogen Energy*, *39*(33), 19270–19276. https://doi.org/10.1016/j.ijhydene.2014.05.098

Li, L., Chen, R., Zhu, X., Wang, H., Wang, Y., Liao, Q., & Wang, D. (2013). Optofluidic microreactors with TiO2-coated fiberglass. *ACS Applied Materials and Interfaces*, *5*(23), 12548–12553. https://doi.org/10.1021/am403842b

Li, L., Tang, D., Song, Y., & Jiang, B. (2018). Dual-film optofluidic microreactor with enhanced light-harvesting for photocatalytic applications. *Chemical Engineering Journal*, *339*(November 2017), 71–77. https://doi.org/10.1016/j.cej.2018.01.074

Liao, W., Wang, N., Wang, T., Xu, J., Han, X., Liu, Z., … Yu, W. (2016). Biomimetic microchannels of planar reactors for optimized photocatalytic efficiency of water purification. *Biomicrofluidics*, *10*(1). https://doi.org/10.1063/1.4942947

Matthews, R. W. (1987). Photooxidation of organic impurities in water using thin films of titanium dioxide. *Journal of Physical Chemistry*, *91*(12), 3328–3333. https://doi.org/10.1021/j100296a044

Nakata, K., & Fujishima, A. (2012). TiO2photocatalysis: Design and applications. *Journal of Photochemistry and Photobiology C: Photochemistry Reviews*, *13*(3), 169–189. https://doi.org/10.1016/j.jphotochemrev.2012.06.001

NASA. (2000). Closing the Loop: Recycling Water and Air in Space 9–12, 1–7. Retrieved from http://www.nasa.gov/audience/foreducators/9-12/features/F_Recycling_on_the_ISS.html.%0Awww.nasa.gov

Pansamut, G., Charinpanitkul, T., & Suriyawong, A. (2013). Removal of hμmic acid by photocatalytic process: Effect of light intensity. *Engineering Journal*, *17*(3), 25–32. https://doi.org/10.4186/ej.2013.17.3.25

Parker, E. R., Thibeault, B. J., Aimi, M. F., Rao, M. P., & MacDonald, N. C. (2005). Inductively Coupled Plasma Etching of Bulk Titanium for MEMS Applications. *Journal of The Electrochemical Society*, *152*(10), C675. https://doi.org/10.1149/1.2006647

Rebiai, S., Bahouh, H., & Sahli, S. (2013). 2-D simulation of dual frequency capacitively coupled heliμm plasma, using COMSOL multiphysics. *IEEE Transactions on Dielectrics and Electrical Insulation*, *20*(5), 1616–1624.

https://doi.org/10.1109/TDEI.2013.6633691

Ren, H., Koshy, P., Chen, W. F., Qi, S., & Sorrell, C. C. (2017). Photocatalytic materials and technologies for air purification. *Journal of Hazardous Materials*, *325*, 340–366. https://doi.org/10.1016/j.jhazmat.2016.08.072

Sakkas, V. A., Arabatzis, I. M., Konstantinou, I. K., Dimou, A. D., Albanis, T. A., & Falaras, P. (2004). Metolachlor photocatalytic degradation using TiO2photocatalysts. *Applied Catalysis B: Environmental*, *49*(3), 195–205. https://doi.org/10.1016/j.apcatb.2003.12.008

Skocaj, M., Filipic, M., Petkovic, J., & Novak, S. (2011). Titanium dioxide in our everyday life; Is it safe? *Radiology and Oncology*, *45*(4), 227–247. https://doi.org/10.2478/v10019-011-0037-0

Song, X.-M., Wu, J.-M., & Yan, M. (2009). Photocatalytic degradation of selected dyes by titania thin films with various nanostructures. *Thin Solid Films*, *517*(15), 4341–4347. https://doi.org/10.1016/j.tsf.2009.02.132

Vangelooven, J., De Malsche, W., De Beeck, J. O., Eghbali, H., Gardeniers, H., & Desmet, G. (2010). Design and evaluation of flow distributors for microfabricated pillar array colμmns. *Lab on a Chip*, *10*(3), 349–356. https://doi.org/10.1039/b916126k

Wang, N., Zhang, X., Wang, Y., Yu, W., & Chan, H. L. W. (2014). Microfluidic reactors for photocatalytic water purification. *Lab on a Chip*, *14*(6), 1074–1082. https://doi.org/10.1039/c3lc51233a

Wang, R., & Hashimoto, K. (n.d.). Light-induced amphiphilic surface.

Wu, C. H., & Chang, C. L. (2006). Decolorization of Reactive Red 2 by advanced oxidation processes: Comparative studies of homogeneous and heterogeneous systems. *Journal of Hazardous Materials*, *128*(2–3), 265–272. https://doi.org/10.1016/j.jhazmat.2005.08.013

Wu, J. M. (2004). Low-temperature preparation of titania nanorods through direct oxidation of titanium with hydrogen peroxide. *Journal of Crystal Growth*, *269*(2–4), 347–355. https://doi.org/10.1016/j.jcrysgro.2004.05.023

Xu, C., Rangaiah, G. P., & Zhao, X. S. (2014). Photocatalytic Degradation of Methylene Blue by Titanium Dioxide: Experimental and Modeling Study. *Industrial & Engineering Chemistry Research*, *53*(38), 14641–14649. https://doi.org/10.1021/ie502367x

Yusuf, A., Garlisi, C., & Palmisano, G. (2018). Overview on microfluidic reactors in photocatalysis: Applications of graphene derivatives. *Catalysis Today*, *315*(November 2017), 79–92. https://doi.org/10.1016/j.cattod.2018.05.041

Zhao, J., Chen, C., & Ma, W. (2005). Photocatalytic Degradation of Organic Pollutants

Under Visible Light Irradiation. *Topics in Catalysis*, *35*(3–4), 269–278. https://doi.org/10.1007/s11244-005-3834-0

Zuruzi, A. S., & MacDonald, N. C. (2005). Facile Fabrication and Integration of Patterned Nanostructured TiO2 for Microsystems Applications. *Advanced Functional Materials*, *15*(3), 396–402. https://doi.org/10.1002/adfm.200400135